Journal of Computational and Applied Mathematics 356 (2019) 248–266

Contents lists available at ScienceDirect

Journal of Computational and Applied Mathematics

journal homepage: www.elsevier.com/locate/cam

Finite element simulation and efficient algorithm for fractional Cahn–Hilliard equation☆

Feng Wang [a], Huanzhen Chen [a,*], Hong Wang [b]

[a] College of Mathematical Science, Shandong Normal University, Jinan, 250014, China
[b] Department of Mathematics, University of South Carolina, Columbia, SC, 29208, USA

ARTICLE INFO

Article history:
Received 30 January 2018
Received in revised form 30 November 2018

Keywords:
Phase field model
Fractional Cahn–Hilliard equation
Linear finite element
Fast BiCG
Efficient algorithm

ABSTRACT

This article is devoted to designing efficient linear finite element algorithm for the fractional Cahn–Hilliard equation, an important and newly proposed phase field model. Combining the advantages of the classic BiCG algorithm and the Toeplitz-like structure of the coefficient matrix, we develop a fast BiCG(FBiCG) algorithm for the linearized scheme to compute numerically the fractional Cahn–Hilliard equation. Our theoretical analysis and numerical experiments demonstrate that the proposed FBiCG reduces the computation cost and the storage to $\mathcal{O}(M \log M)$ and $\mathcal{O}(M)$, possesses the same convergence rates as Newton's algorithm does in space and time, and preserves the energy dissipation and equality laws. The numerical experiments also demonstrate that the FBiCG is almost mass conserved, recognizes accurately the phase separation by a very clear coarse graining process and the influences of different indices r and s of fractional Laplacian and different coefficients K and a on the width of the interfaces.

1. Introduction

Phase field models have become more and more popular in recent years to describe a host of free boundary problems in various research fields. For mathematical descriptions of the thermodynamics and dynamics of two components systems in phase field approach, Cahn and Hilliard [1] in 1958s applied the minimization of the Ginzburg–Landau free energy functional

$$\int_{\Omega} (\frac{1}{2}|\nabla u|^2 + \psi(u))dx$$

with the double-well potential $\psi(u) = \frac{a}{4}u^4 + \frac{b}{2}u^2$, $a > 0$, $b < 0$, and employed Fick's First Law and the continuity equation to formulate the Cahn–Hilliard equation

$$\begin{aligned} &\partial_t u = M\nabla^2 w, \\ &w = -K\nabla^2 u + \psi'(u). \end{aligned} \tag{1.1}$$

☆ This work is supported in part by the National Natural Science Foundation of China under Grant nos. 11471196, 10971254, 11471194 and by the National Science Foundation of USA under Grant Nos. EAR-0934747 and DMS-1216923 and by the OSD/ARO MURI of USA Grant Nos. W911NF-15-1-0562.

* Corresponding author.
E-mail addresses: wangfeng1@stu.sdnu.edu.cn (F. Wang), chhzh@sdnu.edu.cn (H. Chen), hwang@math.sc.edu (H. Wang).

https://doi.org/10.1016/j.cam.2019.01.037
0377-0427/

In phase field models with the double-well potential $\psi(u)$ and $\psi'(u) = f(u) = u(u^2 - 1)$ as $a = 1, b = -1$, $u(x)$ can be viewed as an indicator of the concentration or volume fraction of one fluid A_1 at the location x in the immiscible mixture with the second fluid A_2, that is, if we let $V(A_i)$ denote the volume fraction of fluid A_i, and $V(A_1) + V(A_2) = 1$, then,

$$u_{A_1}(x) = -V(A_1) + V(A_2) = 1 - 2V(A_1).$$

It is easily seen that the range of the indicator u is $[-1, 1]$. Generally, if the double-well potential $\psi(u)$ satisfies $\psi'(u) = f(u) = u(au^2 + b)$ with $a > 0$ and $b < 0$, we can define the weighted volume fraction for fluid A_1 as

$$u_{A_1}(x) = \sqrt{\frac{|b|}{a}}(-V(A_1) + V(A_2)) = \sqrt{\frac{|b|}{a}}(1 - 2V(A_1)).$$

In this case, the range of $u_{A_1}(x)$ is $[-\sqrt{\frac{|b|}{a}}, \sqrt{\frac{|b|}{a}}]$, which depends on the parameters a and b. Some other models such as the Ising ferromagnet, the binary alloys and polymer mixtures, can be found in [1,2].

The key feature of the Cahn–Hilliard equation is that surfaces and interfaces can be described implicitly by continuous scalar field u that takes constant values in the bulk phases and vary continuously but across steeply its diffuse front. Since then, many and many research results on its theories, applications and numerics have been achieved, see the reviews [2–4] and the references cited therein.

If checking carefully the derivation of the Cahn–Hilliard equation (1.1) one could find out that the long-range interactions between particles, which should be expressed as a spatial convolution or a nonlocal integral, was simplified as an integral of local derivative $\frac{1}{2}|\nabla u|^2$ for easy mathematical deduction. This may lose some important information coming from the long-range interactions. Numerous experiments also show that fractional diffusion equations provide an adequate and accurate description of nonlocal transport processes which cannot be modeled properly by second-order diffusion equations [5–9]. Therefore, it could reasonably make physical significance if the Laplacian operator in (1.1) is replaced by its fractional version of Riesz-type potential to form the fractional Cahn–Hilliard equation. In this line, different fractional Cahn–Hilliard models have been proposed and the solvabilities were discussed recently in [10,11], respectively. Fourier spectral method [12] for the fractional Cahn–Hilliard model in [10] and the discontinuous Galerkin method [13] for the linear Caputo-type fractional Cahn–Hilliard model are proposed and analyzed consecutively. As far as we know, there are few works on efficient Galerkin finite element algorithms to simulate numerically the fractional Cahn–Hilliard Models so far.

In this paper, we devote our interest to the efficient finite element algorithm for the fractional Cahn–Hilliard equation proposed in [10],

$$\begin{aligned} &\partial_t u + (-\Delta)^s w(x) = 0, && \text{in} \quad \Omega \times (0, T], \\ &w = K(-\Delta)^r u(x) + au^3 + bu, && \text{in} \quad \Omega \times (0, T], \\ &u(x, 0) = u^0(x), && \text{in} \quad \Omega, \\ &u = w = 0, && \text{in} \quad R\backslash\Omega \times (0, T]. \end{aligned} \tag{1.2}$$

Here $\Omega = (0, 1)$, $0 < r, s < 1$, K and a are positive constants and b negative constant. The fractional Laplace operator $(-\Delta)^l (l = r, s)$ is defined as Riesz-type potential on the whole space R by Definition 2.1 in Section 2. We also notice that the fractional Cahn–Hilliard equation (1.2) will be reduced to the Cahn–Hilliard model (1.1) as $s = r = 1$, the fractional Allen–Cahn equation [14] as $s = 0$ and the fractional porous medium equation [15] as $r = 0$.

The challenges to design a high-performance algorithm are from those: (1) the whole space R as the domain of $(-\Delta)^l$ aggravates the nonlocality of the fractional operators, which makes the computation to be done on an unbounded domain and makes the coefficient matrix resulted from the discrete system being non-sparse; and (2) the algorithm should recognize those physical characteristics: the mass conservation, the energy laws and the phase separation or coarse graining process, as the classic Cahn–Hilliard equation (1.1) does.

The objectives of this paper are to: (1) reduce those computations over unbounded domains to bounded domain computations by using the properties of the operators $(-\Delta)^l$ and the linear finite element spaces, to formulate a nonlinear finite element system; (2) apply the Brouwer's fixed point theorem to prove the solvability of the discrete system for sufficiently small time step, and sharpen the solvability theorem by applying the convex splitting property of the scheme; demonstrate that the discrete solution preserves the energy dissipation and equality laws; (3) combine the merits of the classic BiCG algorithm and the Toeplitz-like structure of the coefficient matrix to design a fast BiCG for the linearized finite element scheme, which reduces the computation cost and the storage to $\mathcal{O}(M \log M)$ and $\mathcal{O}(M)$, respectively; (4) conduct numerical experiments to verify the efficiency of the proposed FBiCG, which show that the FBiCG possesses the ideal convergence rates as Newton's algorithm does in space and time, preserves the energy dissipation and equality laws and almost the mass conservation, and recognizes accurately the phase separation by a very clear coarse graining process. The numerical experiments also test the tunable sharpness, that is, the influences of different indices r and s of fractional Laplacian and different coefficients K and a on the width of the interfaces.

The outline of the article is organized as follows. The first two sections are Introduction and Preliminaries. In Section 3, we construct mixed-type linear finite element procedure. In Section 4, we prove the solvability of the discrete system and demonstrate the discrete solution preserves the energy laws. By combining the Toeplitz-like structure with BiCG method,

we design a fast FBiCG for the linearized finite element scheme to reduce computation cost and storage to $\mathcal{O}(MlogM)$ and $\mathcal{O}(M)$ in Section 5. In Section 6, we perform numerical experiments to demonstrate the performance of the FBiCG algorithm and the finite element procedure.

2. Preliminaries

We first briefly review the definitions and properties of fractional Laplacian operator.

Definition 2.1 ([10,16]). For $u(x) \in \mathcal{S}(R)$, the Schwartz class of the rapidly decaying functions at infinity, the fractional Laplacian operator $(-\Delta)^l$, $0 < l < 1$, is defined by the following Riesz-type potential,

$$(-\Delta)^l u(x) := C_l \lim_{\epsilon \to 0} \int_{R\backslash B(x,\epsilon)} \frac{u(x) - u(y)}{|x-y|^{1+2l}} dy,$$

in which

$$C_l = \frac{4^l l \Gamma(\frac{1}{2} + l)}{\pi^{1/2} \Gamma(1-l)}.$$

Definition 2.2 ([10,17,18]). For $0 < l < 1$, the fractional Sobolev spaces $H^l(R)$ are defined by

$$H^l(R) := \{v \in L^2(R) : \frac{|v(x) - v(y)|^2}{|x-y|^{1+2l}} \in L^1(R \times R)\}$$

and equipped with the norm

$$\|v\|^2_{H^l(R)} := \|v\|^2_{L^2(R)} + \frac{C_l}{2} \int_R \int_R \frac{|v(x) - v(y)|^2}{|x-y|^{1+2l}} dxdy.$$

Let

$$H_0(R) := \{v \in L^2(R) : v = 0 \ a.e. \text{ in } R\backslash\Omega\},$$

$$H_{l,0}(R) := \{v \in H^l(R) : v = 0 \ a.e. \text{ in } R\backslash\Omega\}.$$

We define energy and energy space for the system as follows,

$$\mathbb{E}_r(v) := \frac{K}{2}\|v\|^2_{H_{r,0}} + \frac{a}{4}\int_R v^4 dx + \frac{b}{2}\int_R v^2 dx,$$

$$\mathbb{H}_r(R) := \{v \in H_0(R) : \mathbb{E}_r(v) < +\infty\}.$$

Definition 2.3 ([10]). For $0 < l < 1$. We introduce the operator $T_l : H_{l,0}(R) \to H'_{l,0}(R)$

$$\langle T_l u, v\rangle_{H_{l,0}} := \frac{C_l}{2} \int_R \int_R \frac{(u(x) - u(y))(v(x) - v(y))}{|x-y|^{1+2l}} dxdy, \ \forall u, v \in H_{l,0}.$$

It is easily seen that T_l is a symmetric positive definite operator.

Definition 2.4 ([10]). Let $T > 0$. If $u \in C_w([0,T]; \mathbb{H}_r) \cap C([0,T]; H_0) \cap W^{1,2}(0,T; H'_{r,0})$, $w \in L^2(0,T; H_{s,0})$ satisfies

$$\begin{aligned} &(a) \quad \partial_t u + T_s w = 0, \ \text{ in } H'_{s,0}, \\ &(b) \quad w = KT_r u + au^3 + bu, \ \text{ in } \mathbb{H}'_r, \end{aligned} \tag{2.3}$$

then, the (u, w) is called a weak solution to the Problem (1.2).

Lemma 2.1 ([10]). *If $s, r \in (0,1)$ and $u^0(x) \in \mathbb{E}_r$, the fractional Cahn–Hilliard system (1.2) admits a unique weak solution (u, w) in the sense of Definition 2.4.*

3. Mixed-type linear finite element procedure

In this section, we borrow the weak formulation (2.3) for fractional Cahn–Hilliard equation to construct mixed-type linear finite element procedure.

The weak formulation (2.3) can be rewritten in the following variational form: Find $u \in H_{r,0}$ and $w \in H_{s,0}$ to satisfy

$$\begin{aligned} &(\partial_t u, \sigma) + \langle T_s w, \sigma\rangle = 0, \ \forall \sigma \in H_{s,0}, \\ &(w, v) = K\langle T_r u, v\rangle + a(u^3, v) + b(u, v), \ \forall v \in H_{r,0}, \\ &u(x,0) = u^0(x). \end{aligned} \tag{3.4}$$

For positive integers M and N, we define a uniform partition for $\Omega = [0, 1]$ by $x_i = ih$, $i = 0, 1, 2, \ldots, M$ with $h = 1/M$, and for time interval $[0, T]$ by $t_n = n\tau$ for $n = 0, 1, \ldots, N$ with time step $\tau = T/N$. Upon the space partition, we define the two finite element spaces as

$$V_h = W_h = \{v_h \in C(\Omega) : v_h|_{I_i} \in P_1(I_i), i = 1, 2, \ldots, M; v_h(0) = v_h(1) = 0\},$$

where $P_1(I_i)$ denote the set of polynomials of degree not bigger than 1 on the interval $I_i = (x_{i-1}, x_i)$.

We then define the fully discrete mixed-type finite element procedure of (3.4) as to find $(u_h^n, w_h^n) \in V_h \times W_h$ such that

$$\begin{aligned} &(\frac{u_h^n - u_h^{n-1}}{\tau}, \sigma_h) + \langle T_s w_h^n, \sigma_h\rangle = 0, && \forall\ \sigma_h \in W_h, \\ &(w_h^n, v_h) = K\langle T_r u_h^n, v_h\rangle + a((u_h^n)^3, v_h) + b(u_h^{n-1}, v_h), && \forall\ v_h \in V_h. \end{aligned} \tag{3.5}$$

Let $\varphi_i(x)$ be the inner nodal base function at x_i, $i = 1, 2, \ldots, M-1$ with the structure

$$\varphi_i(x) = \begin{cases} \dfrac{x - x_{i-1}}{h}, & x \in (x_{i-1}, x_i], \\ \dfrac{x_{i+1} - x}{h}, & x \in (x_i, x_{i+1}], \\ 0, & \text{others} \end{cases}$$

and $V_h = W_h = span\{\varphi_i\}_{i=1}^{M-1}$, we then express the numerical solution u_h^n and w_h^n as

$$\begin{aligned} u_h^n(x) &= \sum_{i=1}^{M-1} u_i^n \varphi_i(x) := U^n \cdot \Phi, \\ w_h^n(x) &= \sum_{i=1}^{M-1} w_i^n \varphi_i(x) := W^n \cdot \Phi, \end{aligned} \tag{3.6}$$

where Φ is the linear base vector,

$$U^n = (u_1^n, u_2^n, \ldots, u_{M-1}^n)^T \quad \text{and} \quad W^n = (w_1^n, w_2^n, \ldots, w_{M-1}^n)^T$$

are the unknown vectors.

Using these symbols we rewrite the fully discrete mixed-type finite element procedure (3.5) into the following matrix form,

$$\begin{aligned} &(a) \quad \tau A_s W^n + HU^n = HU^{n-1}, \\ &(b) \quad HW^n - (KA_r + aB)U^n = bHU^{n-1}, \end{aligned} \tag{3.7}$$

where H is a symmetric and positive matrix

$$H = [(\varphi_i, \varphi_j)]_{(M-1)\times(M-1)} = \begin{pmatrix} \frac{2h}{3} & \frac{h}{6} & 0 & \cdots & 0 \\ \frac{h}{6} & \frac{2h}{3} & \frac{h}{6} & \cdots & 0 \\ \vdots & \ddots & \ddots & \ddots & \vdots \\ 0 & \ddots & \ddots & \frac{2h}{3} & \frac{h}{6} \\ 0 & 0 & \cdots & \frac{h}{6} & \frac{2h}{3} \end{pmatrix},$$

$B = [((u_h^n)^2\varphi_i, \varphi_j)]_{(M-1)\times(M-1)}$ is also a symmetric and positive matrix. $A_l, l = r, s$ are Toeplitz matrices with its *ij-entry* $\langle T_l\varphi_i, \varphi_j\rangle$ calculated as follows,

$$\begin{aligned} \langle T_l\varphi_i, \varphi_j\rangle =& \frac{C_l}{2}\int_R\int_R \frac{(\varphi_i(x) - \varphi_i(y))(\varphi_j(x) - \varphi_j(y))}{|x-y|^{1+2l}}dxdy \\ =& \frac{C_l}{2}\left\{\int_\Omega\int_{R\setminus\Omega} \frac{(\varphi_i(x) - \varphi_i(y))(\varphi_j(x) - \varphi_j(y))}{|x-y|^{1+2l}}dxdy\right. \\ &+ \int_{R\setminus\Omega}\int_\Omega \frac{(\varphi_i(x) - \varphi_i(y))(\varphi_j(x) - \varphi_j(y))}{|x-y|^{1+2l}}dxdy \\ &\left.+ \int_\Omega\int_\Omega \frac{(\varphi_i(x) - \varphi_i(y))(\varphi_j(x) - \varphi_j(y))}{|x-y|^{1+2l}}dxdy\right\}. \end{aligned}$$

Applying the properties of the operator $(-\Delta)^l$ to the compact support of linear Lagrange base functions and integrating by parts to reduce these multiple integrals over unbounded domains, we obtain the integrals over finite interval,

$$\begin{aligned}\langle T_l\varphi_i, \varphi_j\rangle =& \frac{C_l}{2}\left\{\int_0^1 \frac{\varphi_i(y)\varphi_j(y)y^{-2l}}{l}dy + \int_0^1 \frac{\varphi_i(y)\varphi_j(y)(1-y)^{-2l}}{l}dy\right.\\ &+\int_0^1\int_0^y \frac{(\varphi_i(x)-\varphi_i(y))(\varphi_j(x)-\varphi_j(y))}{(y-x)^{1+2l}}dxdy\\ &\left.+\int_0^1\int_y^1 \frac{(\varphi_i(x)-\varphi_i(y))(\varphi_j(x)-\varphi_j(y))}{(x-y)^{1+2l}}dxdy\right\},\end{aligned}$$

which possesses the same form as those obtained on Page 7 in [19,20].

After a tedious calculation, we obtain, for $l = 1/2$,

$$\langle T_{\frac{1}{2}}\varphi_i, \varphi_j\rangle = \begin{cases} \frac{C_l}{2}\left\{8\ln(2h) - 8\ln h\right\}, \ |j-i| = 0,\\ \frac{C_l}{2}\left\{7\ln h - 16\ln(2h) + 9\ln(3h)\right\}, \ |j-i| = 1,\\ \frac{C_l}{2}\left\{12\ln(2h) + 8\ln(4h) - 2\ln h - 18\ln(3h)\right\}, \ |j-i| = 2,\\ \frac{C_l}{2}\ \{\ 6m^2\ln(mh) + (m-2)^2\ln(mh-2h)\\ +(m+2)^2\ln(mh+2h) - 4(m-1)^2\ln(mh-h)\\ -4(m+1)^2\ln(mh+h)\ \}, \ |j-i| = m, m = 3,\ldots,M-2.\end{cases}$$

For $l \neq 1/2$, we let $S = l(1-2l)(2-2l)(3-2l)/C_l$ and calculate,

$$\langle T_l\varphi_i, \varphi_j\rangle = \begin{cases} \frac{h^{1-2l}}{S}\left\{-4 + 2^{3-2l}\right\}, |j-i| = 0,\\ \frac{h^{1-2l}}{S}\left\{\frac{7}{2} - 2^{4-2l} + \frac{3^{3-2l}}{2}\right\}, |j-i| = 1,\\ \frac{h^{1-2l}}{S}\ \left\{\ 3(j-i)^{3-2l} - 2(j-i+1)^{3-2l} - 2(j-i-1)^{3-2l}\right.\\ \left.+\frac{(j-i-2)^{3-2l}}{2} + \frac{(j-i+2)^{3-2l}}{2}\ \right\}, |j-i| = m, m = 2,\ldots,M-2.\end{cases}$$

This indicates that the value of the *ij-entry* only depends on the index $m = |j-i|$, the difference between the indices of the i_{th} row and the j_{th} column, which ensures the entries in each descending diagonal are the same. That is, A_l, $l = r, s$ are Toeplitz matrices.

Remark 3.1. To simply display the effectiveness of the methodology we only employ P_1 finite element space in this section, Sections 5 and 6. Certainly, we can use piecewise k_{th} polynomial spaces to pursuit higher convergence rates. In this case, the restriction $V_h = W_h$ is required to form the invertible matrix H through the inner products $(\frac{u_h^n - u_h^{n-1}}{\tau}, \sigma_h)$ and (w_h^n, v_h), and thus the solvability of the finite element scheme (3.5) is ensured.

4. Properties preserved by the finite element procedure

In this section we shall prove the solvability of the nonlinear system (3.7) and demonstrate that the discrete solution preserves energy dissipation and equality laws. It is worthy to point out that the proof in this section is independent of the finite element space index k. For this purpose, we first present two lemmas which play key roles in the proof of the conclusions.

Lemma 4.1. *Assume that $X = (x_1, x_2, \ldots, x_M)^T \in R^M$, $Y = (y_1, y_2, \ldots, y_M)^T \in R^M$ and the matrix $A_{M\times M}$ is symmetric and positive definite. Then,*

$$2X^TA(X-Y) \geq X^TAX - Y^TAY. \tag{4.8}$$

Proof. Noting the symmetry of A and applying a simple calculation, we derive

$$\begin{aligned} 0 &\le (X-Y)^T A(X-Y) \\ &= X^TAX - X^TAY - Y^TAX + Y^TAY \\ &= X^TAX - 2X^TAY + Y^TAY \end{aligned}$$

which yields

$$2X^TAY \le X^TAX + Y^TAY.$$

Then, it follows that

$$\begin{aligned} 2X^TA(X-Y) &= 2X^TAX - 2X^TAY \\ &\ge 2X^TAX - (X^TAX + Y^TAY) \\ &= X^TAX - Y^TAY. \end{aligned}$$

This completes the proof. □

Lemma 4.2. *Assume that $X, Y \in R^M$, E is an invertible $M \times M$ matrix, $P(X)$, $Q(X)$ are $M \times M$ matrices whose matrix norms depend Lipschitz continuously on X, and F_0 and F_1 are given vectors in R^M. Then, the following equation*

$$EY + \tau^2 P(X)X - \tau Q(X)F_0 = F_1 \tag{4.9}$$

can define a mapping $\mathcal{F} : X \in R^M \to Y \in R^M$ such that $\mathcal{F}$ has one and only one fixed point for sufficiently small parameter τ, $0 < \tau < 1$.

Proof. For a given $X \in R^M$, we easily obtain, from (4.9), there exists a unique

$$Y = E^{-1}\{F_1 - (\tau^2 P(X)X - \tau Q(X)F_0)\} \in R^M$$

such that $\mathcal{F}(X) = Y$, which implies that the mapping $\mathcal{F}$ is well-defined and continuous. Further, for $X \in U_{(\cdot,1)} := \{X; \|X - E^{-1}F_1\| \le 1\}$,

$$\begin{aligned} \|Y - E^{-1}F_1\| &= \|E^{-1}\{\tau^2 P(X)X - \tau Q(X)F_0\}\| \\ &\le \tau\|E^{-1}\|\{\|P(X)\|\|X\| + \|Q(X)\|\|F_0\|\} \\ &\le \tau\|E^{-1}\| \sup_{X\in U_{(\cdot,1)}} \{\|P(X)\|\|X\| + \|Q(X)\|\|F_0\|\}, \end{aligned}$$

from which, we have

$$\|Y - E^{-1}F_1\| \le 1, \text{ for } 0 < \tau \le \{\|E^{-1}\| \sup_{X\in U_{(\cdot,1)}} \{\|P(X)\|\|X\| + \|Q(X)\|\|F_0\|\}\}^{-1}.$$

This shows that the mapping $\mathcal{F}$ maps the ball centered at $E^{-1}F_1$ with radius 1 into itself. Thus, the Brouwer's fixed point theorem [21,22] ensures that the mapping $\mathcal{F}$ has at least one fixed point in $U_{(\cdot,1)}$.

The remaining is to show that the fixed point is unique. Let Y_1 and Y_2 in $U_{(\cdot,1)}$ are fixed points, we derive, by subtracting,

$$\begin{aligned} &E(Y_1 - Y_2) = -\tau^2 P(Y_1)Y_1 + \tau Q(Y_1)F_0 + \tau^2 P(Y_2)Y_2 - \tau Q(Y_2)F_0 \\ &= -\tau^2\{P(Y_1)(Y_1 - Y_2) + (P(Y_1) - P(Y_2))Y_2\} + \tau(Q(Y_1) - Q(Y_2))F_0. \end{aligned}$$

After applying the boundedness of $\|E^{-1}\|$ and the Lipschitz continuity of P and Q, we have the following bounds,

$$\|Y_1 - Y_2\| \le C\tau\|Y_1 - Y_2\|,$$

in which the parameter τ can be selected small enough such that $0 < C\tau < \frac{1}{2}$ to force $Y_1 = Y_2$. This completes the proof. □

Theorem 4.3. *There exists a unique solution $(u_h^n, w_h^n) \in V_h \times W_h$ satisfying (3.7) for $n = 1, 2, \ldots, N$ and sufficiently small $\tau > 0$.*

Proof. The proof is based on two steps: the first is to construct, based on the algebraic equation (3.7), a continuous mapping from a ball of R^{M-1} into itself, the second step is to apply Lemma 4.2 and the restriction on τ to prove the mapping has one and only one fixed point.

Noting that H is invertible and thus solving U^n with respect to W^n from (3.7)(a)

$$U^n = U^{n-1} - \tau H^{-1}A_s W^n. \tag{4.10}$$

We recall $u_h^n = U^n \cdot \Phi$ and substitute it into the second term and third term on the left-hand side of (3.7)(b) to eliminate U^n. Then, the obtained matrix B in (3.7)(b) and its entries are expressed by

$$\begin{aligned} ((u_h^n)^2\varphi_i, \varphi_j) &= ((U^n \cdot \Phi)^2\varphi_i, \varphi_j) \\ &= ((U^{n-1} \cdot \Phi - \tau H^{-1}A_s W^n \cdot \Phi)^2\varphi_i, \varphi_j) \end{aligned}$$

and

$$\begin{aligned} BU^n &= (B_1 - 2\tau B_2(W^n) + \tau^2 B_3(W^n))U^n \\ &= (B_1 - 2\tau B_2(W^n) + \tau^2 B_3(W^n))(U^{n-1} - \tau H^{-1}A_s W^n) \end{aligned}$$

with

$$\begin{aligned} &B_1(i,j) = ((U^{n-1}\cdot\Phi)^2\varphi_i, \varphi_j), \\ &B_2(W^n)(i,j) = ((U^{n-1}\cdot\Phi)(H^{-1}A_s W^n\cdot\Phi)\varphi_i, \varphi_j), \\ &B_3(W^n)(i,j) = ((H^{-1}A_s W^n\cdot\Phi)^2\varphi_i, \varphi_j). \end{aligned}$$

The second term is obtained analogously. Collecting the expressions for these two terms we reformulate (3.7)(b) as the following equation with the unknown W^n,

$$EW^n + a\tau^2 P(W^n)W^n - a\tau Q(W^n)U^{n-1} = F_1, \tag{4.11}$$

where

$$\begin{aligned} &E = H + \tau K A_r H^{-1}A_s + a\tau B_1 H^{-1}A_s, \\ &P(W^n) = \tau B_3(W^n)H^{-1}A_s - 2B_2(W^n)H^{-1}A_s, \\ &Q(W^n) = \tau B_3(W^n) - 2B_2(W^n), \\ &F_1 = bHU^{n-1} + KA_r U^{n-1} + aB_1 U^{n-1}. \end{aligned}$$

Noticing that the matrices E, P and Q satisfy the assumptions of Lemma 4.2 we conclude that the mapping $\mathcal{F}$ defined by (4.11) has one and only one fixed point, which is the unique solution W^n to Eq. (3.7)(b), and thus U^n. This completes the proof. □

The restriction for τ being sufficiently small in Theorem 4.3 can be removed by applying its convex splitting property of (3.5) and sharing the argument techniques in [23–27]. From this, a more sharpened result is presented as follows.

Theorem 4.4. *There exists a unique solution $(u_h^n, w_h^n) \in V_h \times W_h$ to the finite element scheme (3.5) for $\tau > 0$.*

Proof. Noticing that H is invertible and thus solving W^n with respect to U^n from (3.7)(a)

$$W^n = \tfrac{1}{\tau}A_s^{-1}H(U^{n-1} - U^n).$$

We substitute it into the second term and third term on the left-hand side of (3.7)(b) to eliminate W^n and obtain

$$\frac{1}{\tau}HA_s^{-1}H(U^n - U^{n-1}) + KA_r U^n + aBU^n + bHU^{n-1} = 0.$$

We then construct the function $F(X)$ with respect to variable $X \in R^{M-1}$,

$$\begin{aligned} F(X) = &\frac{1}{2\tau}X^T HA_s^{-1}HX + \frac{K}{2}X^T A_r X + \frac{a}{2}X^T BX \\ &-\frac{1}{\tau}X^T HA_s^{-1}HU^{n-1} + bX^T HU^{n-1}. \end{aligned}$$

It is easily verified that the Hessian matrix for $F(X)$, which is consisted of $HA_s^{-1}H$, A_r and B, is positive definite, and thus the function F is strictly convex. This implies that the minimizer of $F(X)$ exists uniquely and the minimizer is just the solution to the system

$$\frac{1}{\tau}HA_s^{-1}H(U^n - U^{n-1}) + KA_r U^n + aBU^n + bHU^{n-1} = 0.$$

This completes the proof. □

Theorem 4.5. *The solution $(u_h^n, w_h^n) \in V_h \times W_h$ to the nonlinear system (3.5) satisfies the energy dissipation law, that is, for $n = 1, 2, \ldots, N$,*

$$\mathbb{E}_r(u_h^n) \le \mathbb{E}_r(u_h^{n-1}) \le \cdots \le \mathbb{E}_r(u^0).$$

Proof. Choosing $v_h = w_h^n$ in (3.5)(a), $v_h = \frac{u_h^n - u_h^{n-1}}{\tau}$ in (3.5)(b) and making subtraction, we obtain

$$\begin{aligned} &\langle T_s w_h^n, w_h^n\rangle + K\langle T_r u_h^n, \frac{u_h^n - u_h^{n-1}}{\tau}\rangle \\ &\quad + a((u_h^n)^3, \frac{u_h^n - u_h^{n-1}}{\tau}) + b(u_h^{n-1}, \frac{u_h^n - u_h^{n-1}}{\tau}) = 0. \end{aligned} \tag{4.12}$$

Noting the fact that

$$\|u_h^n\|_{L^2}^2 = (u_h^n, u_h^n) = (U^n)^T H U^n,$$
$$\|u_h^n\|_{H^l}^2 = \langle T_l u^n, u^n\rangle = (U^n)^T A_l U^n, \, l = s, r,$$

and combining Lemma 4.1, we obtain

$$\begin{aligned}(u_h^{n-1}, u_h^{n-1} - u_h^n) &= (U^{n-1})^T H (U^{n-1} - U^n)\\ &\geq \frac{1}{2}((U^{n-1})^T H U^{n-1} - (U^n)^T H U^n),\end{aligned}$$

and

$$\begin{aligned}\langle T_r u_h^n, u_h^n - u_h^{n-1}\rangle &= (U^n)^T A_r (U^n - U^{n-1})\\ &\geq \frac{1}{2}((U^n)^T A_r U^n - (U^{n-1})^T A_r U^{n-1}).\end{aligned}$$

In addition, we use the inequality $ab \leq \frac{1}{2}(a^2 + b^2)$ to derive

$$\begin{aligned}((u_h^n)^3, u_h^n - u_h^{n-1}) &= ((u_h^n)^2, u_h^n(u_h^n - u_h^{n-1}))\\ &\geq \frac{1}{2}((u_h^n)^2, (u_h^n)^2 - (u_h^{n-1})^2)\\ &\geq \frac{1}{4}((u_h^n)^4 - (u_h^{n-1})^4, 1).\end{aligned}$$

Then, substituting these inequalities into (4.12) we derive

$$\begin{aligned}&\tau\|w_h^n\|_{H^s}^2 + \frac{K}{2}(\|u_h^n\|_{H^r}^2 - \|u_h^{n-1}\|_{H^r}^2)\\ &\quad + \frac{a}{4}(\|u_h^n\|_{L^4}^4 - \|u_h^{n-1}\|_{L^4}^4) - \frac{b}{2}(\|u_h^{n-1}\|_{L^2}^2 - \|u_h^n\|_{L^2}^2) \leq 0.\end{aligned}$$

Namely,

$$\begin{aligned}&\tau\|w_h^n\|_{H^s}^2 + \frac{K}{2}\|u_h^n\|_{H^r}^2 + \frac{a}{4}\|u_h^n\|_{L^4}^4 + \frac{b}{2}\|u_h^n\|_{L^2}^2\\ \leq &\frac{K}{2}\|u_h^{n-1}\|_{H^r}^2 + \frac{a}{4}\|u_h^{n-1}\|_{L^4}^4 + \frac{b}{2}\|u_h^{n-1}\|_{L^2}^2.\end{aligned}$$

It follows that $\mathbb{E}_r(u_h^n) \leq \mathbb{E}_r(u_h^{n-1})$ for $n = 1, \ldots, N$. This completes the proof. □

Further, analogous to the deduction in [23–27], we can rewrite (4.12) and replace the energy dissipation law to the following energy equality law under a redefined energy.

Theorem 4.6. *Let $(u_h^n, w_h^n) \in V_h \times W_h$ be the solution to the nonlinear system (3.5). Then, the following new-energy equality law holds for $J = 1, 2, \ldots, N$,*

$$\begin{aligned}&\mathbb{E}_r(u_h^J) + \tau\sum_{n=1}^{J}\|w_h^n\|_s^2 + \frac{K}{2}\sum_{n=1}^{J}\|u_h^n - u_h^{n-1}\|_r^2 - \frac{b}{2}\sum_{n=1}^{J}\|u_h^n - u_h^{n-1}\|^2\\ &\quad + \frac{a}{4}\sum_{n=1}^{J}\|(u_h^n)^2 - (u_h^{n-1})^2\|^2 + \frac{a}{2}\sum_{n=1}^{J}\|u_h^n(u_h^n - u_h^{n-1})\|^2 = \mathbb{E}_r(u_h^0),\end{aligned} \tag{4.13}$$

of which the left hand side is defined as the new-energy expression.

Proof. Rewriting (4.12), we have

$$\begin{aligned}&\tau\|w_h^n\|_s^2 + \frac{K}{2}\|u_h^n\|_r^2 - \frac{K}{2}\|u_h^{n-1}\|_r^2 + \frac{K}{2}\|u_h^n - u_h^{n-1}\|_r^2 + \frac{a}{4}\|u_h^n\|_{L^4}^4\\ &-\frac{a}{4}\|u_h^{n-1}\|_{L^4}^4 + \frac{a}{4}\|(u_h^n)^2 - (u_h^{n-1})^2\|^2 + \frac{a}{4}\|u_h^n(u_h^n - u_h^{n-1})\|^2\\ &+\frac{b}{2}\|u_h^n\|^2 - \frac{b}{2}\|u_h^{n-1}\|^2 - \frac{b}{2}\|u_h^n - u_h^{n-1}\|^2 = 0.\end{aligned}$$

Adding all the terms from $n = 1$ to $n = J$, we derive the following energy equality,

$$\mathbb{E}_r(u_h^J) + \tau \sum_{n=1}^{J} \|w_h^n\|_s^2 + \frac{K}{2} \sum_{n=1}^{J} \|u_h^n - u_h^{n-1}\|_r^2 - \frac{b}{2} \sum_{n=1}^{J} \|u_h^n - u_h^{n-1}\|^2 + \frac{a}{4} \sum_{n=1}^{J} \|(u_h^n)^2 - (u_h^{n-1})^2\|^2 + \frac{a}{2} \sum_{n=1}^{J} \|u_h^n (u_h^n - u_h^{n-1})\|^2 = \mathbb{E}_r(u_h^0).$$

This completes the proof. □

5. Fast bi-conjugate gradient stabilized algorithm (FBiCG)

The finite element scheme (3.5) is a nonlinear scheme, which can be solved through iteration algorithms such as Newton's iteration [28] or through CG algorithm for its linearized version. The linearized scheme can combine itself with FFT and the Toeplitz matrix to develop a fast algorithm naturally. On the other hand, noticing that a direct application of CG algorithm to the coefficient matrix in (3.7) may lead to a rapid growth of iterations, we rewrite the system (3.7) into an equivalent system with the non-symmetric coefficient matrix

$$\widetilde{A} = \begin{pmatrix} A_s & \frac{1}{\tau} H \\ H & -KA_r - aB \end{pmatrix}_{2(M-1)\times 2(M-1)}.$$

and then, we can employ the bi-conjugate gradient stabilized method (BiCG) [29] to solve its linearized version of (3.7).

Therefore, from now on, we linearize the nonlinear equation (3.7) by taking $(u_h^{n-1})^2$ to replace $(u_h^n)^2$ in the matrix B, as commonly used techniques in real computation, and combine the BiCG algorithm, the fast Fourier transform (FFT) [30,31] and the Toeplitz-like structure of the matrix to construct a fast BiCG (FBiCG) to solve the linearized version of (3.7).

By checking BiCG algorithm [29] carefully we find out that what causes the computation cost to be $\mathcal{O}(M^2)$ and storage $\mathcal{O}(M^2)$ per iteration are the matrix–vector multiplications. We hope to modify these matrix–vector multiplications of BiCG algorithm by combining the FFT and the Toeplitz-like structure of the coefficient matrix. The modifications and the related computations are outlined as follows.

Computations for the decomposition of a circulant matrix. A $M \times M$ circulant matrix C can be decomposed as [30,31]

$$C = F_M^{-1} diag(F_M \mathbf{c}) F_M,$$

where $\mathbf{c}$ is the first row vector of C, F_M and F_M^{-1} are the discrete Fourier transform matrix and its inverse with $\mathrm{i}^2 = -1$ and the entries

$$F_M(j, \omega) = exp(-\frac{2\pi \mathrm{i} j\omega}{M}) \text{ and } F_M^{-1}(j, \omega) = \frac{1}{M} exp(\frac{2\pi \mathrm{i} j\omega}{M}), \quad 0 \le j, \omega \le M - 1.$$

Noticing that $\exp(-\frac{2\pi \mathrm{i} j\omega}{M}) = \exp(-\frac{2\pi \mathrm{i} k}{M})$ as $j\omega = k \mod (M)$, $k = 0, 1, \ldots, M-1$ and $j, \omega = 0, \ldots, M-1$, we only need calculate M entries to form the Fourier transform matrix F_M, which needs $\mathcal{O}(M)$ multiplications and additions. Similarly, the computations of F_M^{-1}, the conjugate transpose of F_M, is $\mathcal{O}(M)$, and the computations for $F_M \mathbf{c}$, which can be realized via fast Fourier transform(FFT) for $\mathbf{c}$, is $\mathcal{O}(M \log M)$. Thus, the computational cost for the decomposition of circulant matrix C is $\mathcal{O}(M \log M)$.

Computations for circulant matrix–vector multiplication. According to [30,32,33], the circulant matrix–vector multiplication, which can be implemented by FFT or iFFT, needs $\mathcal{O}(MlogM)$ computational cost and $\mathcal{O}(M)$ memory.

Computations for Toeplitz matrix–vector multiplication. For a $M \times M$ Toeplitz matrix T_M, its each descending diagonal from left to right is a same constant q_i, $i = 0, \pm 1, \ldots \pm(M-1)$, and thus it requires $2M$ storage. On the other hand, it can be embedded into a $2M \times 2M$ circulant matrix C_{2M}[31]. Hence, for a vector $\mathbf{x} \in R^M$, $T_M \mathbf{x}$ can be drawn from $C_{2M}(\mathbf{x}, \mathbf{0})^T$ via

$$C_{2M}\mathbf{X} = \begin{pmatrix} T_M & D_M \\ D_M & T_M \end{pmatrix} \begin{pmatrix} \mathbf{x} \\ \mathbf{0} \end{pmatrix} = \begin{pmatrix} T_M \mathbf{x} \\ D_M \mathbf{x} \end{pmatrix} \tag{5.14}$$

with computational cost $\mathcal{O}(MlogM)$. Here D_M is a Toeplitz matrix whose each descending diagonal from left to right is q_i, $i = 1, \ldots, M-1, 0, 1-M, \ldots, -1$.

Applying the analysis above to the linearized scheme of (3.7) and noting that A_l, $l = r$ and s, are $(M-1) \times (M-1)$ Toeplitz matrices, we can embed A_l into a $2(M-1) \times 2(M-1)$ circulant matrix $C_{2(M-1)}$. The matrix–vector multiplication $A_l \mathbf{x}$ can be drawn from $C_{2(M-1)}(\mathbf{x}, \mathbf{0})^T$ as done in (5.14). This only requires the computational cost $\mathcal{O}(MlogM)$ and storage $\mathcal{O}(M)$. Also, we notice that H and B are $(M-1) \times (M-1)$ tri-diagonal sparse matrices and require the computational cost $\mathcal{O}(M)$ and storage $\mathcal{O}(M)$ for matrix–vector multiplications.

Collecting these deductions above, we modify the traditional BiCG to formulate our fast BiCG algorithm (FBiCG), which is presented sentence by sentence in Algorithm 1, and give the conclusion concerning the efficiency of the FBiCG.

Theorem 5.1. *Compared with BiCG method, the FBiCG proposed in this section reduces computational cost and storage from $\mathcal{O}(M^2)$ and $\mathcal{O}(M^2)$ to $\mathcal{O}(MlogM)$ and $\mathcal{O}(M)$ per iteration.*

Algorithm 1 The FBiCG for $A^k_{2n\times 2n}\mathbf{u}^k = b^{k-1}$(Here, set $n = M-1$)

Input: $u^{(0)} = (u_1^{(0)};\ u_2^{(0)}) = (W^{k-1}; U^{k-1})$

$C_l = (A_l(1,1), \cdots, A_l(n,1), 0, A_l(1,n), \cdots, A_l(1,2))^T,\ l = s, r$

Compute:

$x^{(1)} = \mathrm{FFT}(C_s);\ x^{(2)} = \mathrm{FFT}(C_r)$

$\tilde{W}^0 = (W^0; 0, \cdots, 0);\ \tilde{U}^0 = (U^0; 0, \cdots, 0)$

$v^{(1)} = \mathrm{FFT}(\tilde{W}^0);\ y^{(1)} = v^{(1)}.*x^{(1)};\ z^{(1)} = \mathrm{iFFT}(y^{(1)})$

$v^{(2)} = \mathrm{FFT}(\tilde{U}^0);\ y^{(2)} = v^{(2)}.*x^{(2)};\ z^{(2)} = \mathrm{iFFT}(y^{(2)})$

$w^{(1)} = z^{(1)}(1:n);\ w^{(2)} = z^{(2)}(1:n)$

$r^{(0)} = (r_1^{(0)}; r_2^{(0)}) = (b_1^{k-1} - \tau w^{(1)} - H\cdot U^0; b_2^{k-1} - H\cdot W^0 + w^{(2)} + B\cdot U^0)$

Choose: $\tilde{r} = r^{(0)}$

for $i = 1, 2, \ldots$ **do**

$\rho_{i-1} = \tilde{r}^T r^{(i-1)}$

if $\rho_{i-1} = 0$ **method fails**;

if $i = 1$ **then**

$p^{(i)} = (p_1^{(i)}; p_2^{(i)}) = (r_1^{(i-1)}; r_2^{(i-1)})$

else

$\beta_{i-1} = (\rho_{i-1}/\rho_{i-2})(\alpha_{i-1}/\omega_{i-1})$

$p^{(i)} = r^{(i-1)} + \beta_{i-1}(p^{(i-1)} - \omega_{i-1}v^{(i-1)})$

end if

$\tilde{p}_1^{(i)} = (p_1^{(i)}; 0, \cdots, 0);\ \tilde{p}_2^{(i)} = (p_2^{(i)}; 0, \cdots, 0)$

$v^{(1)} = \mathrm{FFT}(\tilde{p}_1^{(i)});\ y^{(1)} = v^{(1)}.*x^{(1)};\ z^{(1)} = \mathrm{iFFT}(y^{(1)})$

$v^{(2)} = \mathrm{FFT}(\tilde{p}_2^{(i)});\ y^{(2)} = v^{(2)}.*x^{(2)};\ z^{(2)} = \mathrm{iFFT}(y^{(2)})$

$w^{(1)} = z^{(1)}(1:n);\ w^{(2)} = z^{(2)}(1:n)$

$v^{(i)} = (v_1^{(i)}; v_2^{(i)}) = (\tau w^{(1)} + H\cdot p_2^{(i)}; H\cdot p_1^{(i)} - w^{(2)} - B\cdot p_2^{(i)})$

$\alpha_i = \rho_{i-1}/\tilde{r}^T v^{(i)}$

$s = (s_1; s_2) = (r_1^{(i-1)} - \alpha_i v_1^{(i)}; r_2^{(i-1)} - \alpha_i v_2^{(i)})$

If s small enough: $u^{(i)} = u^{(i-1)} + \alpha_i p^{(i)}$

$\tilde{s}_1^{(i)} = (s_1^{(i)}; 0, \cdots, 0);\ \tilde{s}_2^{(i)} = (s_2^{(i)}; 0, \cdots, 0);$

$v^{(1)} = \mathrm{FFT}(\tilde{s}_1^{(i)});\ y^{(1)} = v^{(1)}.*x^{(1)};\ z^{(1)} = \mathrm{iFFT}(y^{(1)})$

$v^{(2)} = \mathrm{FFT}(\tilde{s}_2^{(i)});\ y^{(2)} = v^{(2)}.*x^{(2)};\ z^{(2)} = \mathrm{iFFT}(y^{(2)})$

$w^{(1)} = z^{(1)}(1:n);\ w^{(2)} = z^{(2)}(1:n)$

$t = (t_1; t_2) = (\tau w^{(1)} + H\cdot s_2; H\cdot s_1 - w^{(2)} - B\cdot s_2)$

$\omega_i = t^T s/t^T t$

$u^{(i)} = u^{(i-1)} + \alpha_i p^{(i)} + \omega_i s$

$r^{(i)} = s - \omega_i t$

Check convergence; continue if necessary

end for

Output: $\mathbf{u}^k = u^{(i)}$

6. Numerical experiments

We carry out two types of numerical experiments to investigate the performance of the finite element procedure and the corresponding FBiCG algorithm. The first one is to test the convergence rates and computation cost, then compare the results with other existing algorithms. The second is to test their abilities of the preservation of physical characteristics such as mass conservation, energy laws, phase separation and tunable sharpness. These experiments are implemented by Matlab program on a family computer with configuration: Intel(R) Core(TM) i5-4590 CPU 3.3 GHz and 4 GB RAM.

6.1. Tests on the efficiency of the finite element procedure and FBiCG

Example 1. Assume $\Omega = [0, 1]$, $T = 1$, $K = 1$, $a = 1$, $b = -1$. The analytic solution is prescribed to be

$$u(x,t) = x^2(1-x)^2e^t \in H_0^{2+\gamma}(\Omega) \text{ and } w(x,t) = x(1-x)e^t \in H_0^{1+\gamma}(\Omega)$$

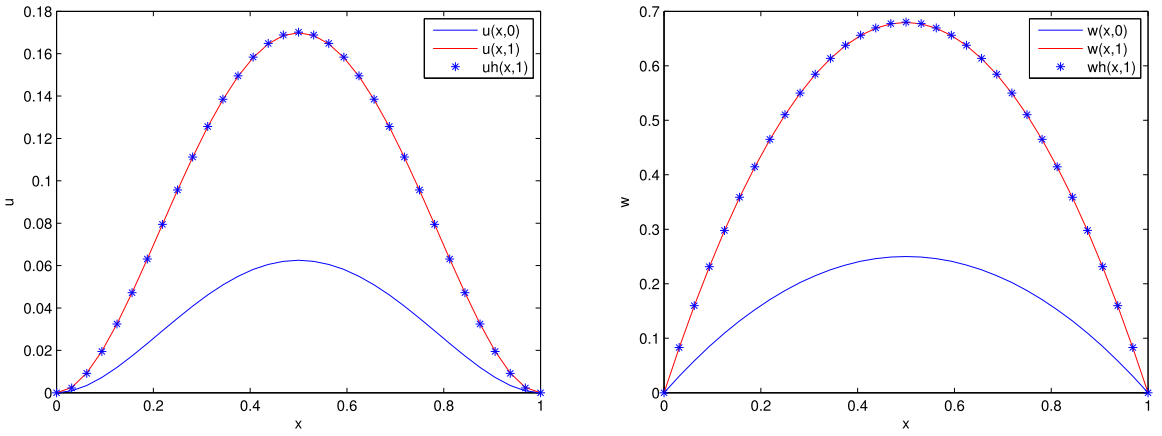

Fig. 1. The initial value, solution and numerical solution at t = 1.

with the initial conditions

$$u(x,0)=x^2(1-x)^2,\quad w(x,0)=x(1-x)$$

and the source terms f_1 and f_2,

$$\begin{aligned}f_1 =&x^2(1-x)^2e^t+C_s\left\{\frac{x^{1-2s}e^t}{2s(1-2s)}+\frac{(1-x)^{1-2s}e^t}{2s(1-2s)}-\frac{x^{2-2s}e^t}{s(1-2s)(2-2s)}\right.\\&\left.-\frac{(1-x)^{2-2s}e^t}{s(1-2s)(2-2s)}\right\},\\f_2 =&x(1-x)e^t-KC_r\left\{\frac{x^{2-2r}e^t}{r(1-2r)(2-2r)}+\frac{(1-x)^{2-2r}e^t}{r(1-2r)(2-2r)}\right.\\&-\frac{6x^{3-2r}e^t}{r(1-2r)(2-2r)(3-2r)}-\frac{6(1-x)^{3-2r}e^t}{r(1-2r)(2-2r)(3-2r)}\\&\left.+\frac{12x^{4-2r}e^t}{r(1-2r)(2-2r)(3-2r)(4-2r)}+\frac{12(1-x)^{4-2r}e^t}{r(1-2r)(2-2r)(3-2r)(4-2r)}\right\}\\&-bx^3(1-x)^3e^{3t}-ax^2(1-x)^2e^{2t}.\end{aligned}$$

Here, $\gamma\in(0,\frac{1}{2})$ can be selected as close to $\frac{1}{2}$ as possible [6–9].

Remark 6.1. Considering the facts that the main aim of this numerical example is to verify its computing efficiency of FBiCG, and the closed form of (1.2) is hardly available, we have to construct such an exact solution by adding the nonzero source terms, without weakening the computing difficulties resulted from the non-locality of the fractional operators. This equation may be thought as a transformed version of the corresponding fractional Cahn–Hilliard equation (1.2) with non-homogeneous boundary conditions. Consequently, the meaningful interval for the transformed solution u is changed to $[0,\frac{e}{16}]$ from $[-1,1]$.

We use this example to test the efficiency on convergence rates in space and time at $t=1$, and to test computation costs up to $t=1$. The calculated results are presented in Fig. 1 and Tables 1–5. Fig. 1 shows the comparisons for the initial value, the exact solution and the numerical solution at $t=1$.

Tables 1 and 2 test the spatial convergence rates for $\|I_hu-u_h\|_{H_{r,0}}$ and $\|I_hw-w_h\|_{H_{s,0}}$ with the time increment $\tau=h^2$ for $r=2/3, s=1/3$ and $\tau=h^3$ for $r=2/3, s=5/6$, the errors between the finite element solution (u_h,w_h) and the linear interpolation (I_hu,I_hw) of the exact solution (u,w), for fixed r and different s. The convergence rates for u are at least 1.7 as $r=\frac{2}{3}, s=\frac{1}{3}$ and 1.4 as $r=\frac{2}{3}, s=\frac{5}{6}$, which are not lower than its interpolation error $\min\{2,2+\gamma\}-r\approx 1.33$. The convergence rates for w are at least 1.76 as $r=\frac{2}{3}, s=\frac{1}{3}$ and 0.74 as $r=\frac{2}{3}, s=\frac{5}{6}$, which are not lower than its interpolation errors $\min\{2,1+\gamma\}-s\approx 1.17$ as $s=\frac{1}{3}$ and 0.67 as $s=\frac{5}{6}$. The results also show that the convergence rates of FBiCG for u and w are almost the same as the Newton's algorithm does.

Tables 3 and 4 show that the temporal convergence rates for u and w are almost equal to 1 for $r=2/3, s=1/3$ and $r=2/3, s=4/5$ with the spatial increment $h=\tau^2$, which are consistent with the theoretical expectations for the backward Euler scheme. This also shows that the temporal convergence rates for u and w are a little bit higher than those of Newton's algorithm.

Table 1
Spatial errors and convergence rates for $\|I_h u - u_h\|_{H_{r,0}}$.

$r = 2/3$	h	Newton's	Rate	FBiCG	Rate
$s = 1/3$	2^{-3}	4.214572448E−03		4.230172050E−03	
	2^{-4}	1.425158899E−03	1.56	1.428530430E−03	1.62
	2^{-5}	4.409662874E−04	1.69	4.416794448E−04	1.73
	2^{-6}	1.317504169E−04	1.74	1.319009008E−04	1.76
	2^{-7}	3.865339671E−05	1.77	3.868534126E−05	1.78
$s = 5/6$	2^{-3}	4.572250166E−03		4.575099755E−03	
	2^{-4}	1.711169460E−03	1.42	1.711545111E−03	1.44
	2^{-5}	5.978203662E−04	1.52	5.978702263E−04	1.53
	2^{-6}	2.140711079E−04	1.48	2.140777889E−04	1.49
	2^{-7}	8.158504985E−05	1.40	8.158590603E−05	1.40

Table 2
Spatial errors and convergence rates for $\|I_h w - w_h\|_{H_{s,0}}$.

$r = 2/3$	h	Newton's	Rate	FBiCG	Rate
$s = 1/3$	2^{-3}	7.945480243E−03		7.916795736E−03	
	2^{-4}	2.135531933E−03	1.89	2.128326044E−03	1.89
	2^{-5}	5.808970898E−04	1.88	5.791599917E−04	1.87
	2^{-6}	1.619746397E−04	1.84	1.615386331E−04	1.83
	2^{-7}	4.754414866E−05	1.77	4.745417998E−05	1.76
$s = 5/6$	2^{-3}	1.125758385E−02		1.125594841E−02	
	2^{-4}	5.329058002E−03	1.08	5.328897215E−03	1.09
	2^{-5}	2.804765013E−03	0.93	2.804750383E−03	0.93
	2^{-6}	1.596474049E−03	0.81	1.596472836E−03	0.81
	2^{-7}	9.534104874E−04	0.74	9.534104178E−04	0.74

Table 3
Temporal errors and convergence rates for $\|I_h u - u_h\|_{H_{r,0}}$.

$r = 2/3$	τ	Newton's	Rate	FBiCG	Rate
$s = 1/3$	1/8	3.685041081E−03		1.991127989E−03	
	1/10	3.036427736E−03	0.87	1.583257182E−03	1.02
	1/12	2.576300059E−03	0.90	1.318463339E−03	1.00
	1/14	2.235275507E−03	0.92	1.131004037E−03	0.99
	1/16	1.973147111E−03	0.93	9.907809489E−04	0.99
$s = 4/5$	1/8	5.494343271E−03		1.044545905E−03	
	1/10	4.532660927E−03	0.86	7.958475702E−04	1.22
	1/12	3.850359950E−03	0.89	6.460511657E−04	1.14
	1/14	3.343923266E−03	0.91	5.450433400E−04	1.10
	1/16	2.954027229E−03	0.93	4.719842117E−04	1.08

Table 4
Temporal errors and rates for $\|I_h w - w_h\|_{H_{s,0}}$.

$r = 2/3$	τ	Newton's	Order	FBiCG	Order
$s = 1/3$	1/8	6.587203592E−03		3.649569961E−03	
	1/10	5.289138492E−03	0.98	2.892873465E−03	1.04
	1/12	4.426584275E−03	0.98	2.403511137E−03	1.02
	1/14	3.808791569E−03	0.98	2.058423962E−03	1.01
	1/16	3.343498632E−03	0.98	1.801080699E−03	1.00
$s = 4/5$	1/8	3.691532710E−03		2.552985169E−03	
	1/10	2.832449976E−03	1.19	1.885641568E−03	1.36
	1/12	2.303708874E−03	1.13	1.491400599E−03	1.29
	1/14	1.944064915E−03	1.10	1.231990030E−03	1.24
	1/16	1.682920953E−03	1.08	1.048677194E−03	1.21

Table 5 tests the efficiency of the FBiCG algorithm. We measure the time for the complete simulation until $t = 1$ with the time increment $\tau = h^2$ for $r = 2/3, s = 1/3$ and $\tau = h^3$ for $r = 2/3, s = 5/6$. We easily see that as the space step h becomes smaller and smaller or equivalently the scale of the equation to be solved becomes larger and larger, the CPU time consumed by the FBiCG is much less than that of the Gauss elimination, Newton's algorithm and the BiCG, and the iterations are the same as BiCG's, which do not scale with M. For example, the CPU time of FBiCG is 0.5 h compared to the Gauss elimination's 14.55 h, Newton's 2.45 h and the BiCG's 6.37 h respectively as $h = 2^{-8}, r = \frac{2}{3}, s = \frac{1}{3}$.

Table 5
Computing efficiency of Gauss, Newton's, BiCG and FBiCG.

$r = 2/3$	h	Gauss	Newton's		BiCG		FBiCG	
		CPU	CPU	Iter.	CPU	Iter.	CPU	Iter.
$s = 1/3$	2^{-3}	0 s	0 s	3	0.05 s	9	0.08 s	9
	2^{-4}	0.05 s	0.05 s	2	0.68 s	17	0.70 s	17
	2^{-5}	1.86 s	0.33 s	2	4.51 s	26	4.86 s	27
	2^{-6}	54.1 s	24.4 s	2	71.1 s	48	32.6 s	47
	2^{-7}	27.5 m	5.72 m	2	22.3 m	73	5.10 m	74
	2^{-8}	14.55 h	2.45 h	2	6.38 h	91	31.7 m	91
$s = 5/6$	2^{-3}	0 s	0.06 s	2	0.44 s	9	0.64 s	9
	2^{-4}	0.95 s	0.75 s	2	7.50 s	15	8.55 s	15
	2^{-5}	58.52 m	11.65 s	2	2.22 m	23	2.06 m	23
	2^{-6}	0.95 h	0.4 h	2	0.73 h	27	0.34 h	27
	2^{-7}	58.7 h	12.22 h	2	18.68 h	30	4.32 h	30

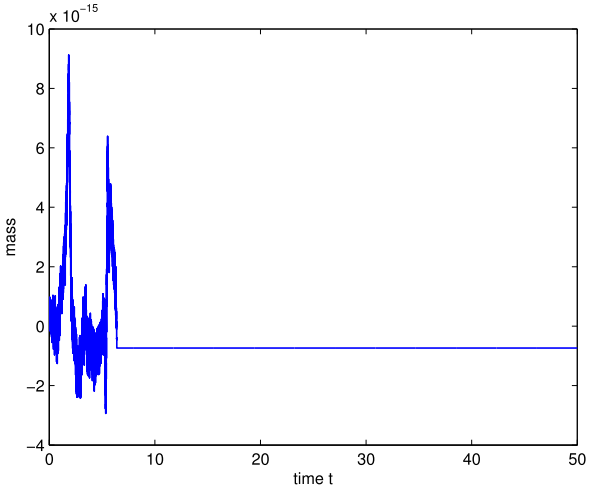

Fig. 2. Mass conservation for $r = 2/3, s = 1/3$.

These results demonstrate that the finite element procedure (3.5) possesses ideal temporal and spatial approximation ability and the FBiCG algorithm evidently improves the computational efficiency compared to the existing algorithms.

6.2. Tests on physical characteristics preserved by the finite element solution

Example 2. Let $b = -1$, $h = 1/100$, $\tau = 1/1200$. The initial function is prescribed to be [34]

$$u(x, 0) = 100x^2(x-1)^2(x-\frac{1}{2}).$$

We use this example by taking $K = 0.002$ and $a = 1$ to test the abilities of the finite element solution of (3.5) to preserve the mass conservation, energy laws and phase separation for fixed s and r. The corresponding numerical results are plotted in Figs. 2–9. We also use this example by taking different r, s, K, a to test the influences of these parameters on the interface width. The numerical results are presented by Figs. 10–14, respectively.

Mass Conservation. The classic Cahn–Hilliard equation (1.1) is derived by the continuity equation and therefore the mass conservation is preserved. However, if we multiply the first equation of its fractional version (1.2) by the constant function 1 and then integrate, we find out that $\langle T_s w, 1\rangle \neq 0$ may destroy the mass balance due to the operator being defined over R. This may reflect a fact in physics that a small amount of the mass may be transported to $R\backslash\Omega$ through the fractional flux. Nevertheless, we do think that its fractional version (1.2) should inherit, at least in part, this very important physical property—mass conservation. In fact, our numerical results plotted in Figs. 2 and 3 also confirm this conjecture. Fig. 2 shows that the mass jumps in the scale of 10^{-15} at the very beginning, and then begins to be conserved after $t \approx 6.4$ s. In Fig. 3, the mass conservation is going to be preserved after $t \approx 5.83$ s. This demonstrates that the finite element solution to (3.5) almost preserves the mass conservation and the fractional Cahn–Hilliard equation inherits partially the mass conservation properties from its integer version (1.1).

Energy Law. The energy laws are very important physical properties to reflect the energy conversion among different substances. It has been proved in [10] that the energy dissipation law holds for the fractional Cahn–Hilliard equation

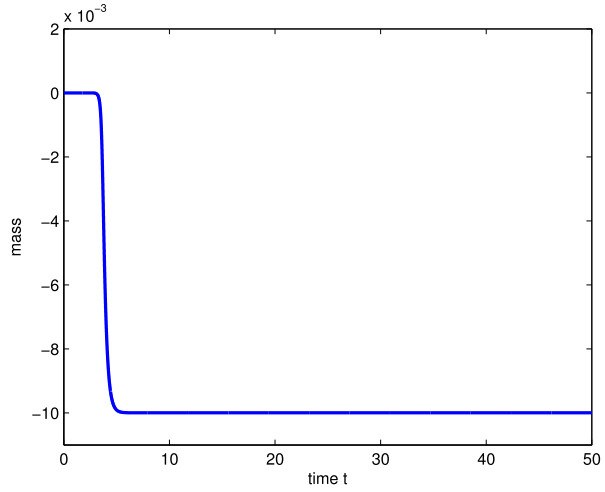

Fig. 3. Mass conservation for $r = 3/5, s = 2/3$.

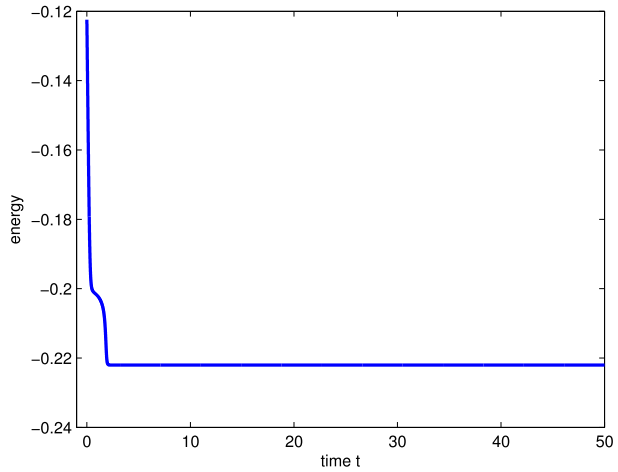

Fig. 4. Energy dissipation for $r = 2/3, s = 1/3$.

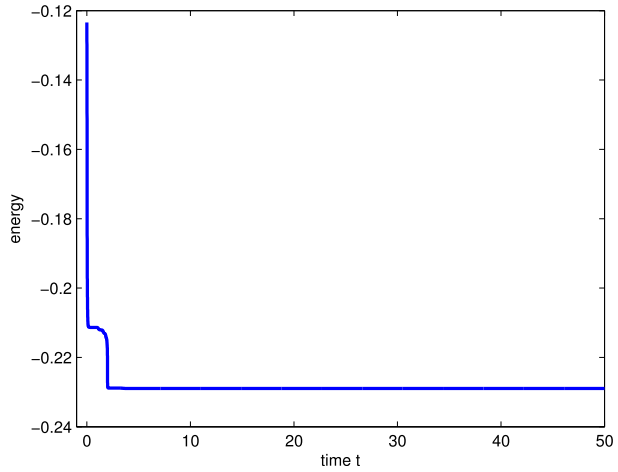

Fig. 5. Energy dissipation for $r = 3/5, s = 2/3$.

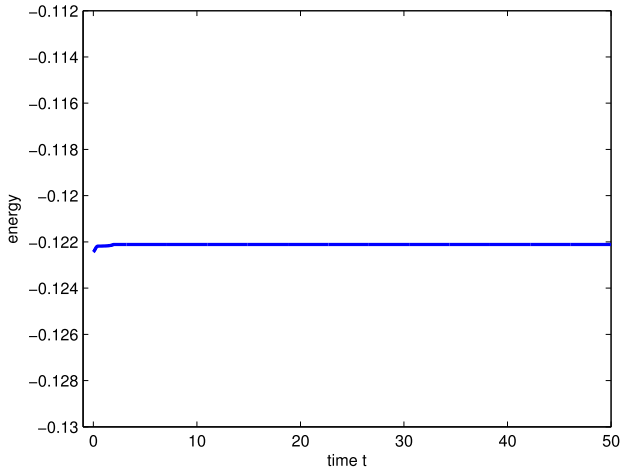

Fig. 6. Energy conservation for $r = 2/3, s = 1/3$.

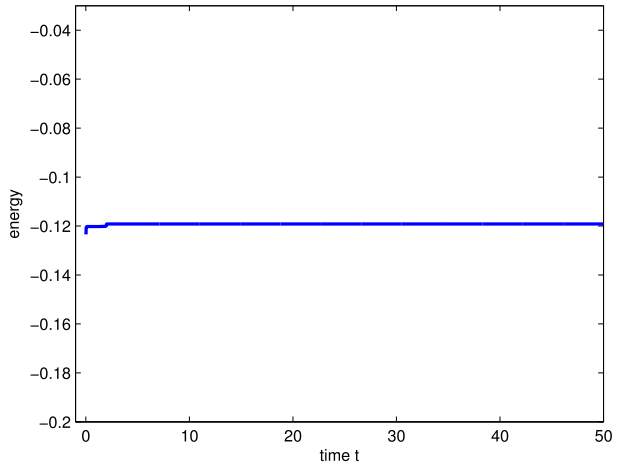

Fig. 7. Energy conservation for $r = 3/5, s = 2/3$.

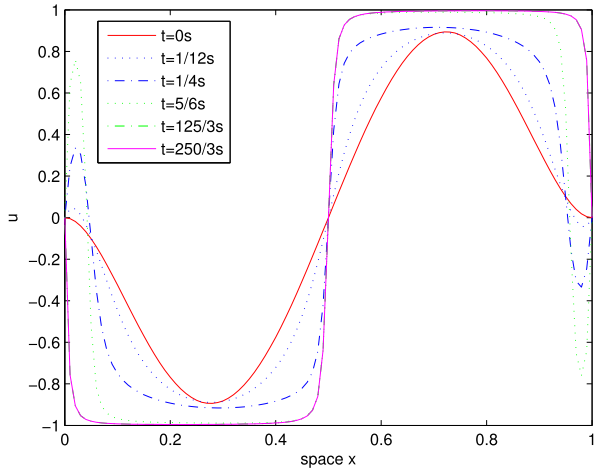

Fig. 8. Coarse graining for $r = 2/3, s = 1/3$.

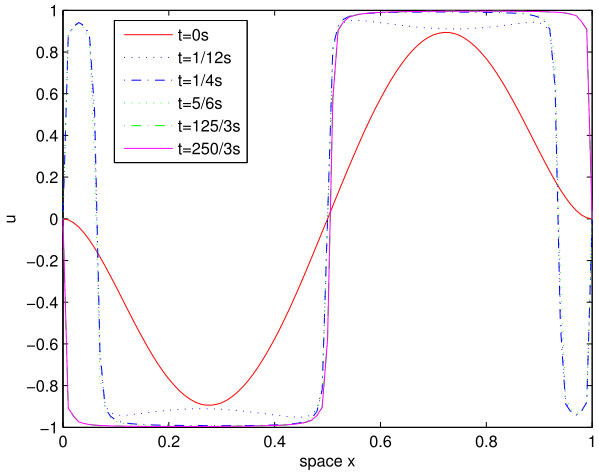

Fig. 9. Coarse graining for $r = 3/5, s = 2/3$.

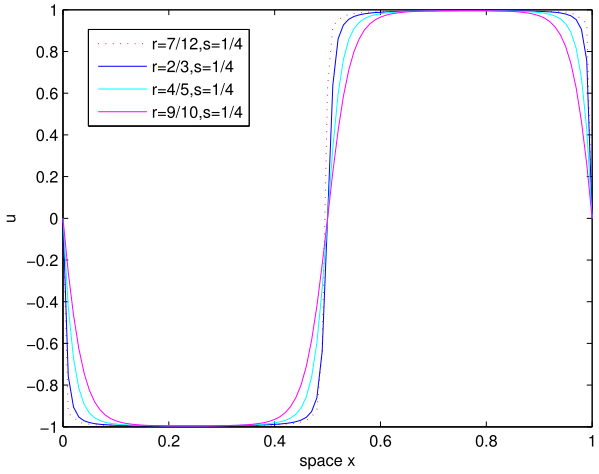

Fig. 10. Tunable sharpness for fixed s at $t = 166.7$.

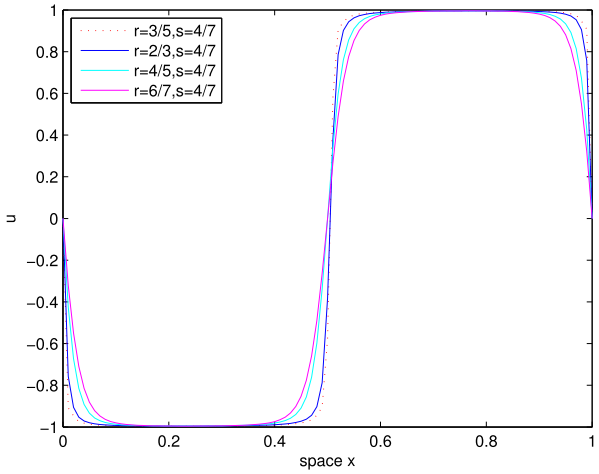

Fig. 11. Tunable sharpness for fixed s at $t = 166.7$.

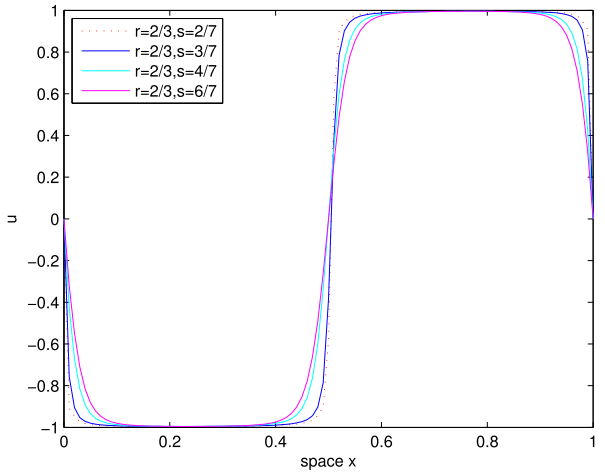

Fig. 12. Tunable sharpness for fixed r at $t = 166.7$.

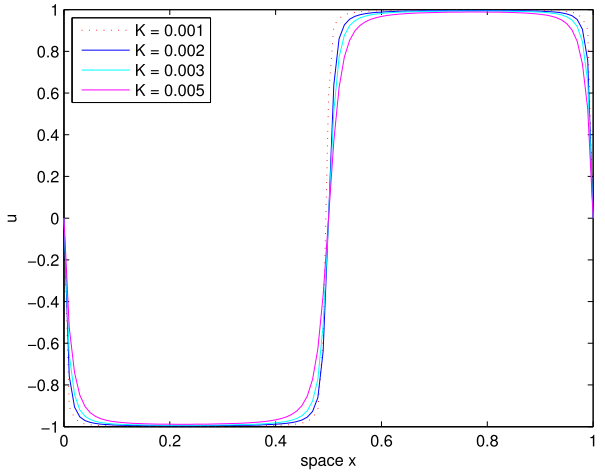

Fig. 13. Tunable sharpness for fixed K at $t = 166.7$.

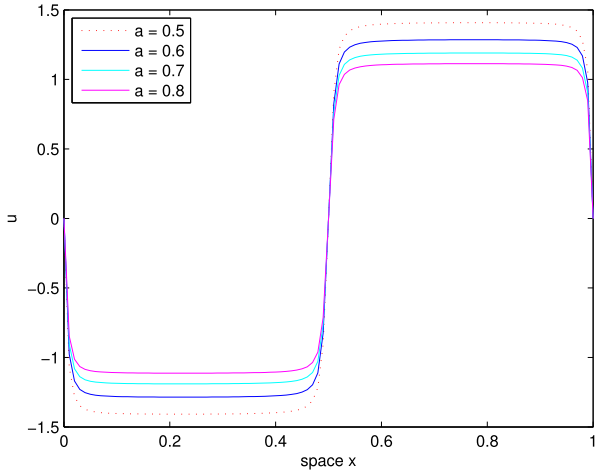

Fig. 14. Tunable sharpness for fixed a at $t = 166.7$.

and the finite element procedure (3.5) also possesses these energy dissipation law by Theorem 4.5. We further prove the new-energy conservation law under the redefined energy in Theorem 4.6. Our numerical results sketched in Figs. 4 and 5 show that the total energy decreases with time for different indices of r and s. The results in Figs. 6 and 7 show that the new-energy is kept constant in the scale of 10^{-4}. The numerical experiments confirm again that the energy dissipation and equality laws are preserved by the finite element procedure (3.5) and the fractional Cahn–Hilliard equation (1.2).

Phase Separation. The spatial patterns with different r and s represented by the numerical solutions in Figs. 8 and 9 correspond to the physical phenomenon of a coarse graining process as the time increases. We can see that the final numerical solutions of Figs. 8 and 9 correspond exactly to the monotone and smooth solution that is the global minimizer of the total energy, which means that the phase separation is achieved.

Tunable Sharpness. "Tunable sharpness" refers to the influences of the index of temporal fractional derivative on the width of the interfaces in the simulation for the fractional Allen–Cahn equation [35,36]. Here we borrow this name to describe the influences of the indices r and s on the width of the interfaces or the influences of the diffusion coefficient K and the double-well potential parameter a on the width of the interfaces, at $t = 166.7$ respectively.

The effect of parameters r and s on interface width. We test the tunable sharpness for fixed $s = \frac{1}{4}$ or $s = \frac{4}{7}$ against different r by Figs. 10 and 11, respectively. The numerical results demonstrate that as r increases, the corresponding widths of the equilibrium state are becoming wider a bit. The numerical results in Fig. 12 show that, for fixed r, the width of the interface becomes wider and wider as s increases.

The effect of parameters K and a on interface width. Figs. 13 and 14 display the effect of parameters K and a on interface width, respectively. As K or a increases, the interface thickness, proportional to $\sqrt{Ka}$, becomes wider and the absolute value of equilibrium state is $\sqrt{\frac{|b|}{a}}$. These are in accordance with the observations of the integer Cahn–Hilliard equation.

These results are reasonable since the diffusive ability of the components becomes stronger as r, s or K, a increase.

Acknowledgments

The authors would like to express their sincere thanks to the anonymous referees for their valuable comments and suggestions, which greatly improved the quality of this paper.

References

[1] J.W. Cahn, J.E. Hilliard, Free energy of a non-uniform system I: Interfacial free energy, J. Chem. Phys. 28 (1958) 258–264.
[2] M. Plapp, Phase-field models, in: CISM Courses and Lectures, Vol. 538, 2012, pp. 129–175.
[3] J. Shen, Modeling and numerical approximation of two-phase incompressible flows by a phase-field appoach, Multiscale Modeling Anal. Mater. Simul. (2012) 147–195.
[4] Y. Wang, J. Li, Phase filed modeling of defects and deformation, Acta Mater. 58 (2010) 1212–1235.
[5] F. Liu, V. Anh, I. Turner, Numerical solution of the space fractional Fokker–Planck equation, J. Comput. Appl. Math. 166 (2004) 209–219.
[6] H.Z. Chen, H. Wang, Numerical simulation for conservative fractional diffusion equations by an expanded mixed formulation, J. Comput. Appl. Math. 296 (2016) 480–498.
[7] L.L. Jia, H.Z. Chen, H. Wang, Mixed-type galerkin variational principle and numerical simulation for a generalized nonlocal elastic model, J. Sci. Comput. 71 (2017) 660–681.
[8] V.J. Ervin, J.P. Roop, Variational formulation for the sationary fractional advection dispersion equation, Numer. Methods Partial Differ. Equ. 22 (3) (2010) 558–576.
[9] Y.S. Li, H.Z. Chen, H. Wang, A mixed-type Galerkin variational formulation and fast algorithms for variable-coefficient fractional diffusion equations, Math. Methods Appl. Sci. 40 (2017) 5018–5034.
[10] G. Akagi, G. Schimperna, A. Segatti, Fractional Cahn-Hilliard Allen-Cahn and porous medium equations, J. Differential Equations 261 (6) (2016), 2935–2985.
[11] H. Abels, S. Bosia, M. Grasselli, Cahn-Hilliard equation with nonlocal singular free energies, Ann. Mat. Pura Appl. 194 (4) (2015) 1071–1106.
[12] Z.F. Weng, S.Y. Zhai, X.L. Feng, A Fourier spectral method for fractional-in-space Cahn-Hilliard equation, Appl. Math. Model. 42 (2017) 462–477.
[13] T. Aboelenen, H.M. El-Hawary, A high-order nodal discontinuous Galerkin method for a linearized fractional Cahn-Hilliard equation, Comput. Math. Appl. 73 (2017) 1197–1217.
[14] Y. Nec, A.A. Nepomnyashchy, A.A. Golovin, Front-type solutions of fractional Allen-Cahn euqaitons, Physica D 237 (2008) 3237–3251.
[15] A. de Pablo, F. Quirós, A. Rodríguez, J.L. Vázquez, A general fractional porous medium equation, Comm. Pure Appl. Math. 65 (2012) 1242–1284.
[16] E. Di Nezza, G. Palatucci, E. Valdinoci, Hitchiker's guide to the fractional Sobolev spaces, Bull. Sci. Math. 136 (2012) 521–573.
[17] J.-L. Lions, E. Magenes, Problèmes aux Limites non Homogènes et Applications, vol. 1, in: Travaux et Recherches Mathématiques, vol. 17, Dunod, Paris, 1968.
[18] R.A. Adams, J.J.F. Fournier, Sobolev Spaces, second ed., Elsevier, Amsterdam, 2003.
[19] M. Ainsworth, C. Glusa, Aspects of an adaptive finite element method for the fractional Laplacian: A priori and a posteriori error estimates, efficient implementation and multigrid solver, Comput. Methods Appl. Mech. Engrg. (2017).
[20] G. Acosta, F.M. Bersetche, J.P. Borthagaray, A short FE implementation for a 2d homogeneous Dirichlet problem of a fractional Laplacian, Comput. Math. Appl. (2016) 784–816.
[21] L.E.J. Brouwer, Beweis der invarianz der dimensionenzahl, Math. Ann. 70 (2) (1911) 161–165.
[22] V.L. Lstratescu, Fixed Point Theory, Reidel, 1981.
[23] A.C. Aristotelous, O. Karakashian, S.M. Wise, A mixed discontinuous Galerkin, convex splitting scheme for a modified Cahn-Hilliard equation and an efficient nonlinear multigrid solver, Discrete Contin. Dyn. Syst. Ser. B 18 (9) (2014) 2211–2238.
[24] J. Shen, Yang, et al., Numerical approximations of Allen-Cahn and Cahn-Hilliard equations, Discrete Contin. Dyn. Syst. 28 (4) (2010) 1669–1691.
[25] J. Xu, Y. Li, S. Wu, et al., On the Stability and Accuracy of Partially and Fully Implicit Schemes for Phase Field Modeling 2016.
[26] X. Feng, Fully discrete finite element approximations of the Navier–Stokes-Cahn-Hilliard diffuse interface model for two-phase fluid flows, SIAM J. Numer. Anal. 44 (3) (2006) 1049–1072.

[27] X. Feng, Y. Li, Y. Xing, Analysis of mixed interior penalty discontinuous Galerkin methods for the Cahn-Hilliard equation and the Hele-Shaw flow 2015, 54(2):1102-1121.
[28] R.L. Burden, J.D. Faires, Numerical Analysis, Thomson Learning, New York, 2001.
[29] R. Fletcher, Conjugate gradient methods for indefinite system, Numer. Anal. (1976) 73–89.
[30] P.J. Davis, Circulant Matrices, Wiley-Intersciences, New York, 1979.
[31] R.M. Gray, Toeplitz and circulant matrices: a review, Found. Trends Commun. Inform. Theory 2 (3) (2006) 155–239.
[32] K.X. Wang, H. Wang, A fast characteristic finite difference method for fractional advection-diffusion equations, Adv. Water. Resour. 34 (2011) 810–816.
[33] S.L. Lei, H.W. Sun, A circulant preconditioner for fractional diffusion equations, J. Comput. Phys. 242 (2013) 715–725.
[34] D. Furihata, A stable and conservative finite difference scheme for the Cahn-Hilliard equation, Mumer. Math. 87 (4) (2001) 675–699.
[35] F. Song, C. Xu, G.E. Karniadakis, A fractional phase-field model for two-phase flows with tunable sharpness: Algorithms and simulations, Comput. Methods Appl. Mech. Engrg. 305 (2016) 376–404.
[36] Z. Li, H. Wang, D. Yang, A space–time fractional phase-field model with tunable sharpness and decay behavior and its efficient numerical simulation, J. Comput. Phys. 347 (2017) 20–38.